Effect of Anisotropic Velocity Structure on Acoustic Emission Source Location during True-Triaxial Deformation Experiments

Civil Engineering
UNIVERSITY OF TORONTO

M. G. (Sherveen) Tabari , S.D. Goodfellow, and R.P. Young

European Geosciences Union General Assembly 2016
Vienna | Austria | 17–22 April 2016

EGU2016-9303
April 20, 2016. Poster Number: X2.98.
Session Title: EMRP1.4/SM2.5/TS1.6,
Earthquakes: from slow to fast, from the field to the laboratory.

http://civil.engineering.utoronto.ca/staff/professors/paul-young/ *Email: sherveen.m.g.tabari@alum.utoronto.ca* *LinkedIn: sherveentabari* *University of Toronto, Mining Building, Toronto, Ontario, Canada*

Introduction

Although true-triaxial testing (TTT) of rocks is now more extensive worldwide, stress-induced heterogeneity due to the existence of several loading boundary effects is not usually accounted for and simplified anisotropic models are used. This study focuses on the enhanced anisotropic velocity structure to improve acoustic emission (AE) analysis for an enhanced interpretation of induced fracturing. Data from a TTT on an 80 mm-side cubic sample of Fontainebleau sandstone is used in this study to evaluate the methodology. At different stages of the experiment the True-Triaxial Geophysical Imaging Cell (TTGIC), armed with an ultrasonic and AE monitoring system, performed several velocity surveys to image velocity structure of the sample. Going beyond a hydrostatic stress state (poro-elastic phase), the rock sample went through a non-dilatational elastic phase, a dilatational non-damaging elasto-plastic phase containing initial AE activity and finally a dilatational and damaging elasto-plastic phase up to the failure point. The experiment was divided into these phases based on the information obtained from strain, velocity and AE streaming data. Analysis of the ultrasonic velocity survey data discovered that a homogeneous anisotropic core in the center of the sample is formed with ellipsoidal symmetry under the standard polyaxial setup. Location of the transducer shots were improved by implementation of different velocity models for the sample starting from isotropic and homogeneous models going toward anisotropic and heterogeneous models. The transducer shot locations showed a major improvement after the velocity model corrections had been applied especially at the final phase of the experiment. This location improvement validated our velocity model at the final phase of the experiment consisting lower-velocity zones bearing partially saturated fractures. The ellipsoidal anisotropic velocity model was also verified at the core of the cubic rock specimen by AE event location of transducer shots. AE of the rock during the whole experiment recorded by the surrounding transducers were investigated by location methods developed for anisotropic heterogeneous medium where, the M-shape fracture pattern was observed. AE events occurred in the vicinity of the dilation pseudo-boundaries where, a relatively large velocity gradient was formed and along parallel fractures in the σ1/σ2 plane. This research is contributing to enhanced AE interpretation of fracture growth processes in the rock under laboratory true-triaxial stress conditions.

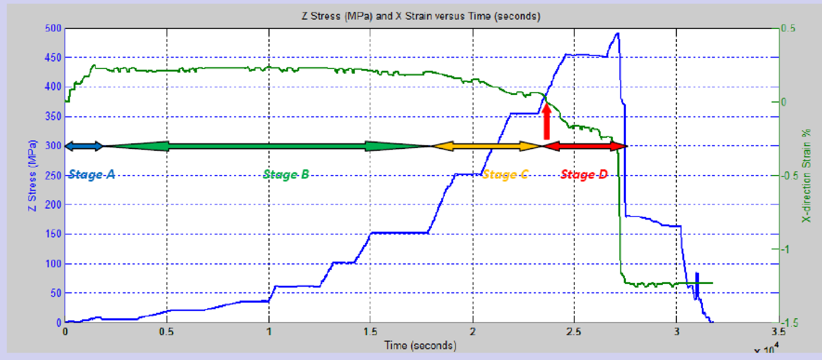

Schematic view of different stages of the Polyaxial test on Fontainbelau Sandstone:
Top: Evolution of main principal stress (blue) and strain in the X-axis (green) under fixed σ_2=35 (Mpa) and σ_3=5 (Mpa). Bottom: : Evolution of main principal stress (blue), cumulative Acoustic Emission Activity (green)

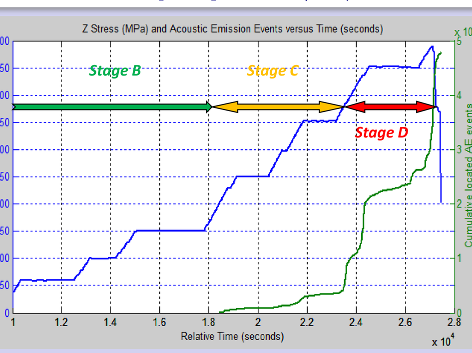

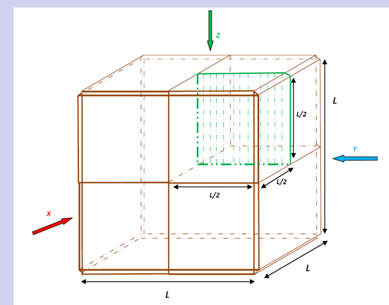

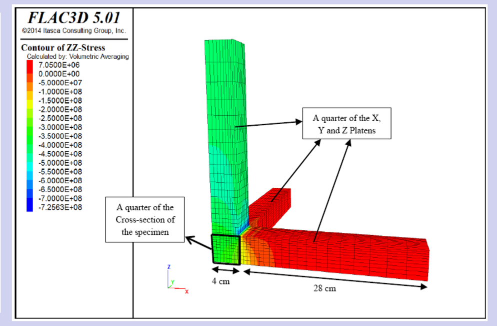

Cross-section of the TTT system and FLAC3D Modeling of Stress distribution at the center of the rock along the X and Y directions for measurement of the lower-stressed zone pseudo-boundaries in the minimum and intermediate principal stress directions

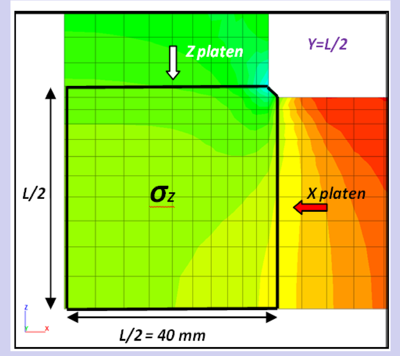

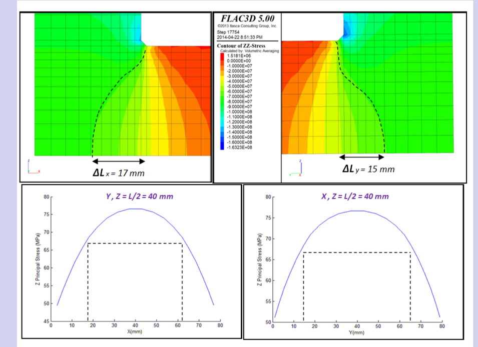

Transducer to Transducer Velocity Survey

There are 18 transducers located on the six platens surrounding the cubic rock specimen that both record the acoustic emission events and perform ultrasonic velocity surveys during the experiment. Each of the 18 transducers emits P wave pulses into the rock, and the other 17 transducers receive and record it. The figure below on the left demonstrates the locations of the transducers as well as the 153 ray-paths between the transducers in our laboratory configuration. The figure on the right represents a stereonet diagram of the apparent P wave velocities from a T-to-T survey. The velocities computed for each ray-path hitting the lower hemisphere are projected and plotted on a horizontal circular area called stereonets at the point corresponding to the trend and plunge of that ray-path. The vertical direction of the stereonet (0° plunge) corresponds to the Z axis direction of the sample which is the main principal stress direction causing the maximum velocity direction.

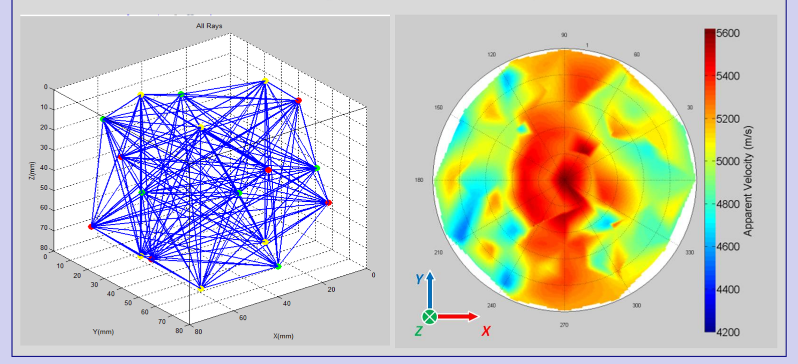

Ray-path Travel-time in Ellipsoidal Media

When isotropic elastic media is triaxially stressed, constitute a special subset of orthorhombic media, called "ellipsoidal media". Ellipsoidal symmetry is a degenerate case of orthorhombic symmetry but with 6 independent elastic parameters instead of 9. The relation between the components of the velocity vector within an ellipsoid in the three principal directions is,

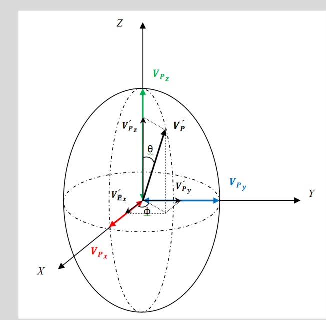

$$\frac{V_{p_x}'^2}{V_{p_x}^2}+\frac{V_{p_y}'^2}{V_{p_y}^2}+\frac{V_{p_z}'^2}{V_{p_z}^2}=1,\quad \frac{V_{p_x}}{V_{p_z}}=\alpha,\quad \frac{V_{p_y}}{V_{p_z}}=\beta$$

The velocity vector can be decomposed in the Cartesian coordinate system as below,

$$V_{p_x}'=V_p\cos\varphi\sin\theta,\quad V_{p_y}'=V_p\sin\varphi\sin\theta,\quad V_{p_z}'=V_p\cos\theta \qquad V_p=\sqrt{V_x'^2+V_y'^2+V_z'^2}$$

Combining and Simplifying the equations above for a medium divided into grid cells (i),

$$\frac{(V_{p_i}\cos\varphi_i\sin\theta_i)^2}{V_{p_{x_i}}^2}+\frac{(V_{p_i}\sin\varphi_i\sin\theta_i)^2}{V_{p_{y_i}}^2}+\frac{(V_{p_i}\cos\theta_i)^2}{V_{p_{z_i}}^2}=1 \Rightarrow V_{p_i}^2\left(\frac{(\cos\varphi_i\sin\theta_i)^2}{\alpha^2V_{p_{z_i}}^2}+\frac{(\sin\varphi_i\sin\theta_i)^2}{\beta^2V_{p_{z_i}}^2}+\frac{(\cos\theta_i)^2}{V_{p_{z_i}}^2}\right)=1$$

Thus, components of the local velocity vector for any ray-path with a certain direction of propagation in each probing grid cell can separately be obtained through the following equation based upon the semi-principal axes lengths ratios, α and β,

$$\begin{cases} V_{p_{z_i}}=V_{p_i}\sqrt{\dfrac{(\cos\varphi_i\sin\theta_i)^2}{\alpha^2}+\dfrac{(\sin\varphi_i\sin\theta_i)^2}{\beta^2}+(\cos\theta_i)^2} \\ V_{p_{x_i}}=\alpha V_{p_{z_i}} \\ V_{p_{y_i}}=\beta V_{p_{z_i}} \end{cases}$$

Shear and Compressional Wave Velocities in the Minimum and Intermediate Principal Stress Direction from the P-S1-S2 Surveys

In LS stands for Lower-Stress Zone, and the index "c" presents the central part of the rock that is more compressed and intact.

$$V_{13}^{(LS)}=\left[\frac{L}{2\Delta l_1}\left(\frac{1}{V_{13}}-\left(\frac{L-2\Delta l_1}{L}\right)\frac{1}{V_{31}}\right)\right]^{-1}$$

$$V_{23}^{(LS)}=\left[\frac{L}{2\Delta l_2}\left(\frac{1}{V_{23}}-\left(\frac{L-2\Delta l_2}{L}\right)\frac{1}{V_{32}}\right)\right]^{-1}$$

There are two boundary zones considered for each of the minimum and intermediate principal stress directions and, there is no boundary zones assumed in the main principal stress direction.

All the velocities in different central and near boundary zones are calculated based on the velocity ratios between the main principal direction and the other two principal directions.

P and S Wave Ultrasonic Velocity Measurements in the Central Compacted zone and the Lower-Stressed Zones of the Cubic Rock Sample in Three Principal Directions from P-S1-S2 Velocity Surveys

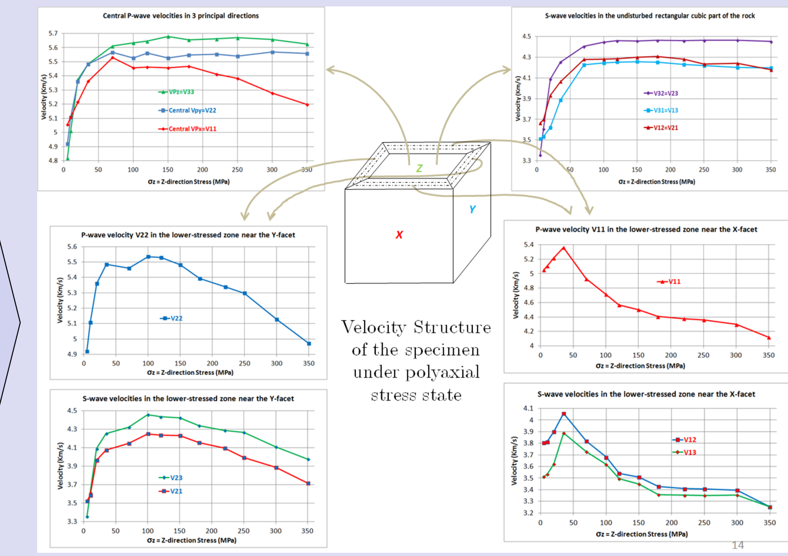

Source Location with different Isotropic/Anisotropic and Homogeneous/Heterogeneous Velocity Models

An AE event occurs at an unknown time t_s and at an unknown position of the source as (x_s, y_s, z_s). If the receiver transducers located at detect the AE events at real arrival-time data, this arrival-time as the observed or recorded data will depend on the origin time and the travel-time between the source and the receiver. By knowing the velocity structure, the synthetic arrival-times at the receivers can be computed from a hypothetical model vector composed of the source location and origin time. For example, in an isotropic homogeneous velocity structure, the synthetic arrival-time data is:

$$d_i=T_i(x_s,x_i)+t_s=\frac{((x_i^2-x_s^2)+(y_i^2-y_s^2)+(z_i^2-z_s^2))^{\frac{1}{2}}}{v}+t_s$$

Then, an inversion method can be used to find a model that the consequent synthetic arrival-times fit the real arrival-times better. For an anisotropic homogeneous velocity structure, there is a different velocity (v_i) for each seismic ray that will depend on the orientation of ray vector demonstrated by dip and strike. The synthetic arrival-time will be,

$$d_i=\frac{((x_i^2-x_s^2)+(y_i^2-y_s^2)+(z_i^2-z_s^2))^{\frac{1}{2}}}{v_i}+t_s \qquad \text{Where,}\quad v_i=\frac{v_z}{\sqrt{\frac{(\cos\varphi_i\sin\theta_i)^2}{\alpha^2}+\frac{(\sin\varphi_i\sin\theta_i)^2}{\beta^2}+(\cos\theta_i)^2}}$$

In an anisotropic heterogeneous velocity structure, each block also has different velocities for the same seismic ray. If v_q^i is corresponded to velocity of ray i with arrival-time d_i that the ith sensor detects when passing through the qth block, then the synthetic arrival-time is:

$$d_i=\sum_q\frac{dist_q^i}{v_q^i}+t_s$$

Where $dist_q^i$ is the distance that the ith ray travels through the qth block. $dist_q^i$ is a portion of the total length of the ray vector between source and receiver and leads to defining a constant c_q^i relative to the corresponding block velocity v_q^i in order to write the following equation

$$dist_q^i=c_q^i((x_i^2-x_s^2)+(y_i^2-y_s^2)+(z_i^2-z_s^2))^{\frac{1}{2}},\quad \sum_q c_q^i=1$$

Thus, the synthetic arrival-time can be calculated as

$$d_i=((x_i^2-x_s^2)+(y_i^2-y_s^2)+(z_i^2-z_s^2))^{\frac{1}{2}}\sum_q\frac{c_k^i}{v_q^i}+t_s$$

Collapsing Grid Search and Location Methodology

Since our goal was not to develop a fast and cost efficient event location, but to examine the effect of velocity structure on accuracy of the location results, we chose the simplest location method, which is grid search. In a grid search, the test specimen is discretized into a particular grid, and the travel-times from any point in the grid to each sensor are calculated. We collapsed the grid size down to a final range of cubic window with 0.1 mm space intervals in each of the three orthogonal directions as well as a range of time window with 0.1 (μs) time intervals while choosing the AE hypocenter locations by finding the **minimum time residual**, given by,

where, t_i **is the computed P wave travel-time and** d_i **is the real P wave travel-time data.**

$$R=\sqrt{\sum_{i=1}^{18}(t_i-d_i)^2}$$

First, a **single-valued isotropic homogeneous velocity model** with a constant velocity of 5500 (m/s) was used during the experiment for transducer survey shot locations at different stages of the experiment. **20 different transducer survey travel-time data were analyzed at various stress states during the experiment.** The figure below shows the mean time residual (R) for the 16 shot locations as well as the mean location misfits between all the shots at each of the transducer surveys.

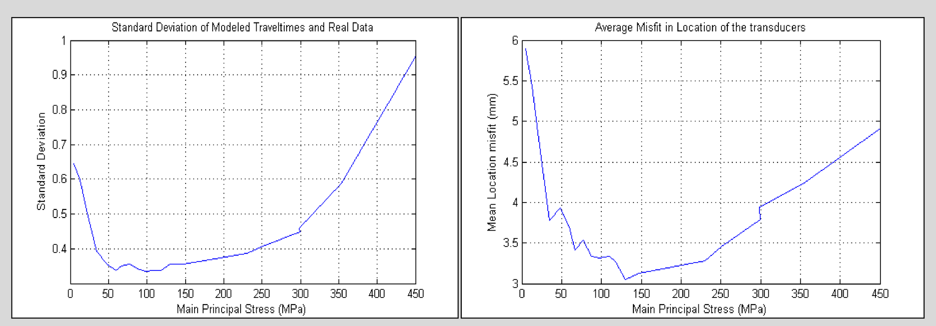

In the next step, we used a different value for the isotropic homogeneous velocity model. The **varying isotropic homogeneous velocity model** used for transducer survey shot locations at different stages of the experiment is provided in the table below.

#	Main Principal stress (MPa) at different Transducers Surveys	Main Principal stress (MPa) at different P-S1-S2 surveys	P Wave Velocity (km/s) from P-S1-S2 Survey in all directions for the homogeneous model
1	5	5	4.93
2	13	10	5.07
3	20	20	5.32
⋮			
19	353	350	5.38
20	450	470	5.17

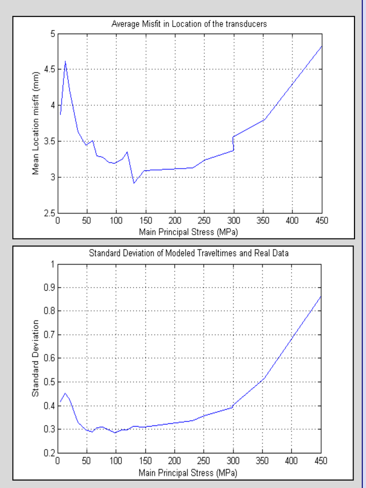

In the next step, an **anisotropic homogeneous P wave velocity model** was used for transducer survey shot locations at different stages of the experiment. Time residual (R) for the 16 shot locations as well as the mean location misfits graph is shown on the right.

#	Main Principal Stress (MPa) at Different Transducer surveys	Main Principal Stress (MPa) at Different P-S1-S2 surveys	P Wave Velocity (km/s) from P-S1-S2 Survey in direction of: Main Principal Stress	Intermediate Principal Stress	Minimum Principal Stress
1	5	5	4.82	4.92	5.06
2	13	10	5.01	5.11	5.11
⋮					
19	353	350	5.71	5.40	5.04
20	450	470	5.68	5.25	4.60

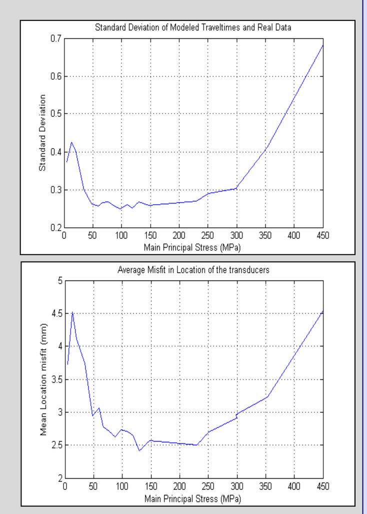

The **anisotropic (ellipsoidal) heterogeneous velocity model** used for transducer-to-transducer survey shot locations at different stages of the experiment is given in the table below. The velocities are obtained from the P and S wave ultrasonic velocity measurements in the central compacted zone and the lower-stressed zones of the cubic rock sample in three principal directions from P-S1-S2 velocity surveys shown above. We applied this structure all over the test including all A to D stages of the experiment.
The two graphs signify that the AE source locations using the anisotropic heterogeneous model has not made a significant change in results compared to using the transversely isotropic or ellipsoidal homogeneous velocity model in our laboratory scale rock specimen. However, the results in the final velocity survey are remarkably different with almost 2 mm improvement in accuracy of the transducer locations.

#	Stress at Transducer Surveys (MPa)	Stress at P-S1-S2 Surveys (MPa)	Center X	Center Y	Center Z	Y facets X	Y facets Y	Y facets Z	X facets X	X facets Y	X facets Z
1	5	5	5.06	4.92	4.82	5.06	4.92	4.82	5.06	4.92	4.82
2	13	10	5.11	5.11	5.01	5.11	5.11	5.01	5.11	5.11	5.01
⋮											
19	353	350	5.20	5.56	5.63	4.66	4.97	5.03	4.12	4.40	4.45
20	450	470	4.63	5.27	5.56	4.15	4.71	4.97	3.67	4.17	4.40

(P Wave Velocity (km/s) from P-S1-S2 Survey)

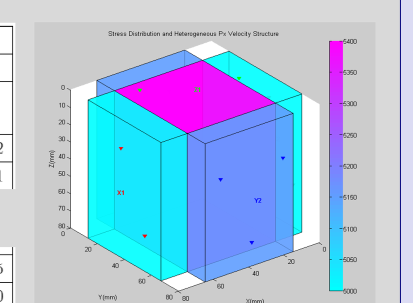

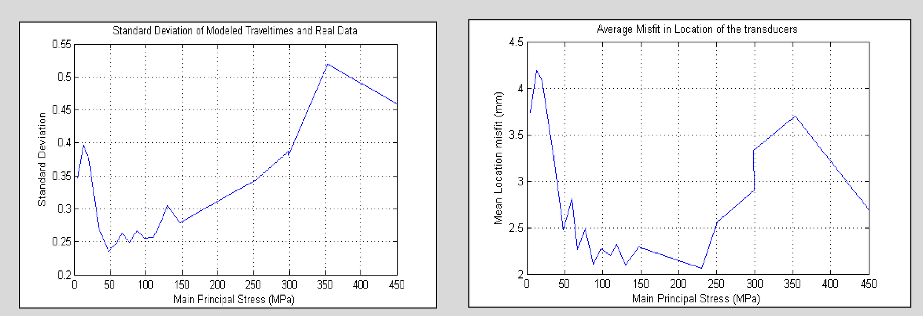

3D as well as the XoY, XoZ and YoZ cross sectional source location images of 58,000 AE activities during the experiment.

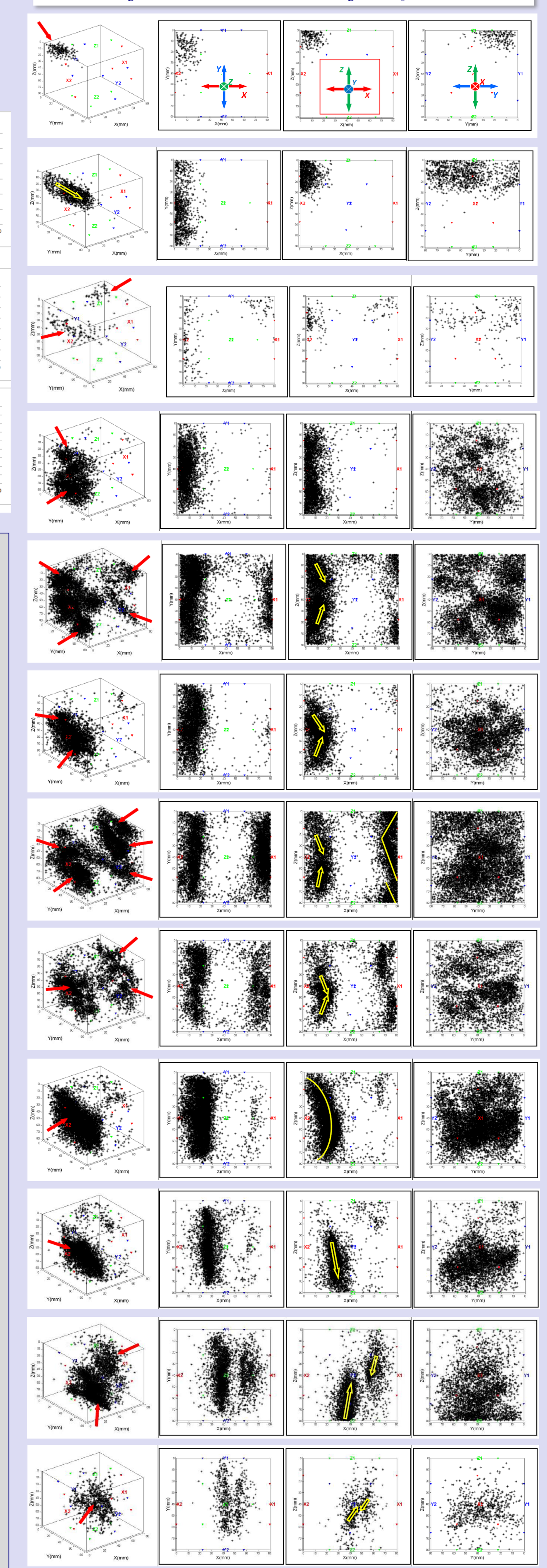

AE source location patterns versus CT scan image of the XoZ cross section of the rock at the middle of the Y axis

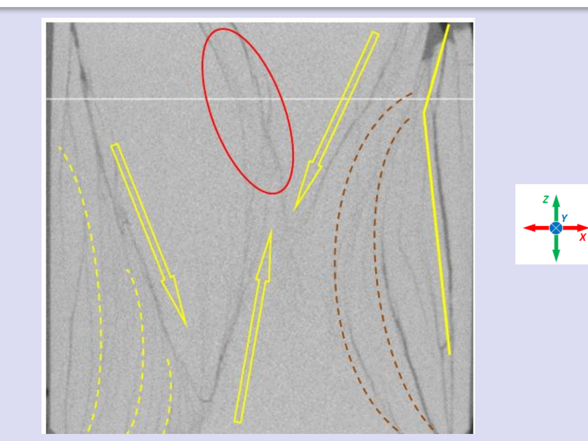

Discussion

In the transducer location results, the calculated source time zero also affects the resultant time residual (R). Therefore, sometimes the location may have even bigger misfit in location but with a relatively smaller time residual (R). The diameter of the transducer surface is about 2 mm and as a result, a minimum of 2 mm uncertainty in locations of the shot transducers is inevitable and reasonable. Although the location results in the anisotropic heterogeneous model did not make a significant change compared to the transversely isotropic or even to the ellipsoidal homogeneous velocity model, however, the final transducer positions in the final velocity survey at stage D were recovered with almost 2 mm improvement. This indicates that the anisotropic heterogeneous velocity structure with dilatancy pseudo-boundaries is entirely effective after the weakening near the facets in the minimum principal stress direction by the deformational AE activities.

The features in yellow as well as the semi-curves in brown shown in the CT scan image of the rock were almost observed by the AE source locations. In total, we were able to recover a good deal of the fracturing process by the AE source locations especially with the aid of the continuous waveforms from the AE streaming system.

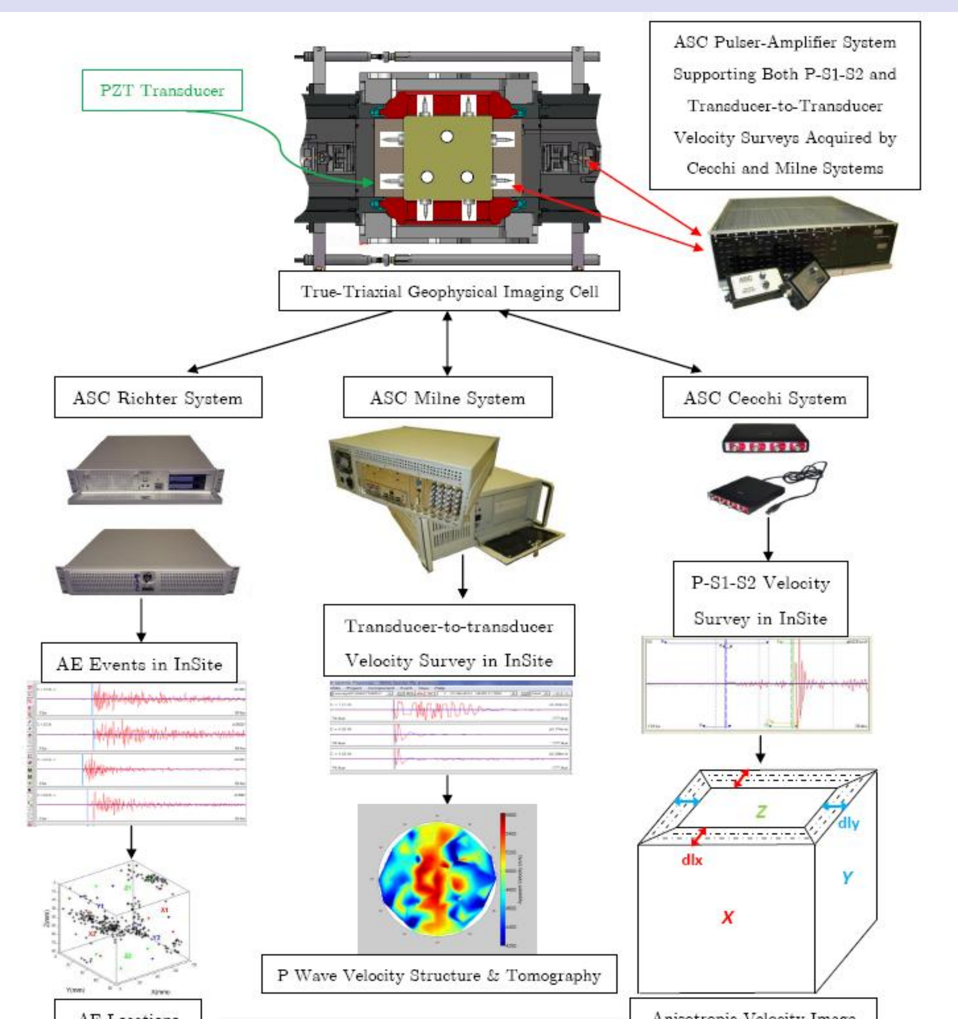

Schematic Flowchart of Data Acquisition and Processing

Acknowledgements

We acknowledge Dr. M.H.B. Nasseri for supervising the experimental setup as well as Laszlo Lombos for manufacturing the Polyaxial Geophysical Imaging Cell.

Key References

1. Tabari, M. G. (2015). Time-lapse Ultrasonic Imaging of Elastic Anisotropy in Saturated Sandstone under Polyaxial Stress State (Doctoral dissertation, University of Toronto).
2. Nasseri, M. H. B., Goodfellow, S.D., Young, R. P., & Lombos, L. (2014) 3D transport and acoustic properties of Fontainebleau sandstone during true-triaxial deformation experiments, International Journal of Rock Mechanics and Mining Sciences, Volume 69, July 2014, Pages 1-18